JTTEE5 17:517–524
DOI: 10.1007/s11666-008-9204-2
1059-9630/$19.00 © ASM International

Transient Flowfield Characteristics of Polycarbonate Plasma Discharge from Pulse-Powered Electrothermal Gun Operation

Kyoungjin Kim

(Submitted November 19, 2007; in revised form March 11, 2008)

An electrothermal gun is the device that produces high-temperature and high-velocity plasma vapor using high current pulsed power and has a potential to be an efficient method for producing a variety of nanomaterials. Pulsed plasma discharge from the electrothermal gun into the open air has been investigated numerically, and the time-dependent inviscid gas dynamics equations are solved for the two-dimensional computational domain including electrothermal gun and the open-air space using flux-corrected transport (FCT) scheme. The modeling of the Joule heating and the mass ablation from the bore wall are incorporated in the computation. The computational results yield the details of the plasma discharge behavior inside and outside the capillary bore including choked condition at the bore exit and complex shock structure of external plasma discharge. The flow structure of freely expanding plasma discharge in the open air is essentially the highly underexpanded supersonic jet featuring Mach disk, barrel shock, contact surface, and spherical blast wave. Compared to the experiments, the numerical simulation agrees well with the experimental data such as the capillary mass ablation and shock structure of the plasma jet.

Keywords electrothermal gun, numerical modeling, plasma spray, underexpanded jet

1. Introduction

An electrothermal gun or electrothermal-chemical gun is powered by high-magnitude current pulses to produce a pulsed plasma discharge. This device has been originally developed to improve the combustion rate of the solid propellants for the acceleration of the projectile by high-temperature, high-pressure, and high-velocity plasma jet as an alternative to the conventional chemical igniters (Ref 1). The process employs the high power discharge of electrical energy to vaporize the solid materials of capillary bore and electrodes, and the eroded vapor is subsequently ionized to form a dense plasma during the duration of a high current discharge. The vapor plasma then exits the open end of the bore to create a high-velocity, high-temperature, high-pressure, and highly ionized external plasma jet into the open or closed chamber.

Especially in the last decade or so, there have been several experimental and theoretical investigations in the area of plasma discharge technology using pulsed power. The United States Army Research Laboratory (ARL) has maintained an extensive program to investigate this technology with a goal to improve the ignition of solid propellant. White et al. (Ref 1) and Nusca et al. (Ref 2) conducted experiments for the open-air plasma discharge which showed the typical formation of an underexpanded jet. The experimental program has been carried out for years at The University of Texas at Austin (Ref 3, 4). Using the small-scale plasma igniter with polycarbonate liner, the open-air experiments were conducted to study the characteristics of the freely expanding plasma jet.

In the theoretical studies on the interior conditions of electrothermal gun, there have been several different approaches depending on the degree of simplification. Powell and Zielinski (Ref 5, 6) introduced a simple quasi-steady isothermal model and it provides excellent predictions despite its simplicity. Raja et al. (Ref 7) assumed that the flow is quasi-steady in their one-dimensional modeling. In contrast, Powell and Zielinski (Ref 5, 6), Zaghloul et al. (Ref 8), and Kim (Ref 9) performed the theoretical analysis using time-dependent one-dimensional models. For the plasma discharge in the open air, Nusca et al. (Ref 2) carried out numerical study by employing the time-dependent multidimensional CFD code, FAST3D. In their research, the exit conditions of the electrothermal gun were calculated by a time-dependent one-dimensional code and supplied as the boundary conditions at the bore exit plane into the expanding plasma flow simulation, and their results showed good agreement with the their measured plasma jet structure.

Kyoungjin Kim, School of Mechanical Engineering, Kumoh National Institute of Technology, 1 Yangho, Gumi, Gyeongbuk 730-701, South Korea. Contact e-mail: kimkj@kumoh.ac.kr.

This process has a potential to be another efficient method for thermal plasma jet spray coating where, presently, a DC arc or RF discharge are the popular heat sources for producing a thermal plasma jet. The other possible applications might be the nanoparticle coating using nanosized materials of various kinds, which can be produced by reacting the plasma vapor with background gas before the plasma jet reaches the coating target. This investigation presents the numerical simulation of the plasma discharge into the open air from electrothermal gun operations by utilizing the time-dependent computation of gas dynamics in the two-dimensional axisymmetric domain that includes both interior and exterior of the electrothermal gun. The computational results are presented and compared with the corresponding measurements.

2. Numerical Modeling of External Plasma Discharge

2.1 Electrothermal Gun

Figure 1 shows a schematic diagram of the electrothermal gun which was used in the experimental work by Center for Aeromechanics Research at The University of Texas at Austin (Ref 3, 4). The electrothermal gun is driven by a pulse-forming network (PFN), which consists of the capacitor banks (C), inductors (L), resistors (R), and the ignition switch. Both the capacitors and the inductors can be varied to apply variable current, energy, voltage, and pulse duration time. The capillary bore of the electrothermal gun is 3.1 mm in diameter ($D = 2r_b$) and 30 mm in length, and made of polycarbonate (Lexan, $C_{16}H_{14}O_3$). The electrodes were made of copper-tungsten alloy to resist the material erosion from the plasma. A fine copper fuse wire was used between the anode and cathode to initiate the plasma discharge.

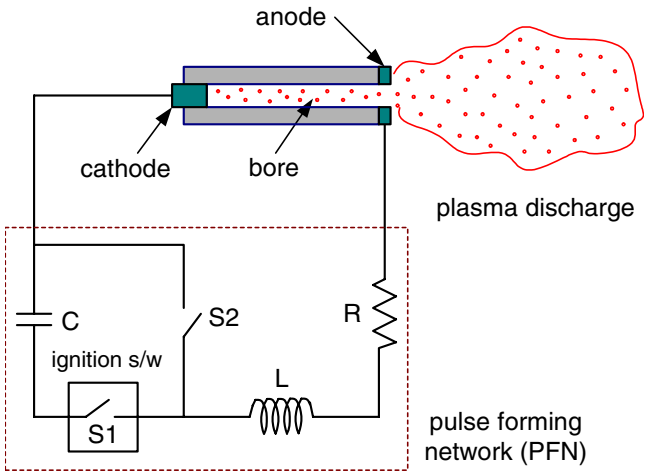

Fig. 1 Schematic diagram of electrothermal gun

When the ignition switch (S1) is closed, the discharge of stored electrical energy from the capacitor bank is then initiated, and the capillary bore and the fuse wire establish a current path for the discharge. Then, the ablating polycarbonate bore is subsequently vaporized and ionized due to intense Joule heating. The resulting plasma flow rapidly expands from an open end of the bore into the exterior region. The PFN consists of 251 μF capacitor and 26 μH inductor and the energy initially stored in the capacitor bank was approximately 3.1 kJ with the initial capacitor voltage of 5 kV. Figure 2 shows the recorded traces of the electrical current during the plasma discharge. The peak current of approximately 4.6 kA was obtained at 110 μs, and the pulse duration is approximately 250 μs.

The typical flow pattern of the freely expanding plasma discharge of high pressure from the capillary bore is a supersonic underexpanded jet, which is illustrated in Fig. 3. Due to the Joule heating from the electrical discharge and the mass addition from the bore wall, plasma flow velocity reaches sonic speed and the flow becomes choked at the bore exit. Mach disk is a nearly planar normal shock that resides in front of bore exit and its location depends on the pressure ratio of the bore exit to the background gas. The barrel shock forms at the side as the supersonic flow adjusts to the background state. For the evolving plasma discharge, the additional features include the hemispherical blast wave which propagates through the background gas and the expanding contact surface which divides the plasma and the background gas. This type of flowfield can be observed in some situations of impulsive supersonic jet such as gun muzzle blast (Ref 10). Also, Djakov and Hermoch (Ref 11) showed a similar pattern of erosion plasma jet formation from arc electrodes. Turbulent mixing could be considerable at the contact surface but it will not alter the inviscid nature of the shock structure substantially for the period of pulse duration.

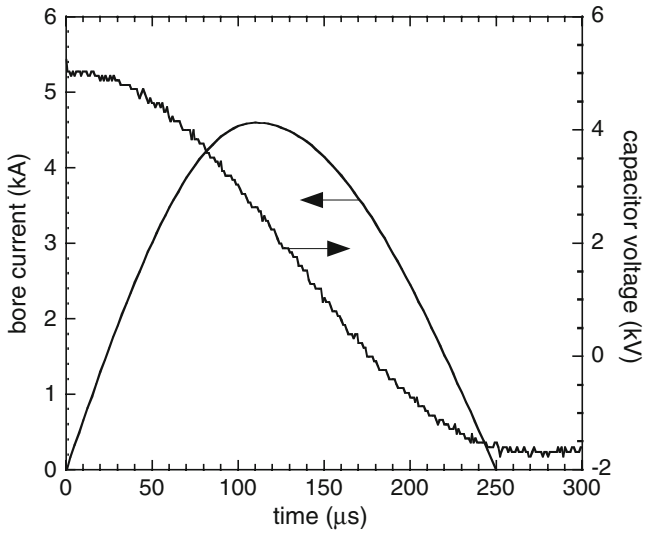

Fig. 2 Traces of recorded electrical current across the capillary bore and capacitor voltage during the electrothermal gun firing with the initial capacitor voltage of 5 kV (Ref 3, 4)

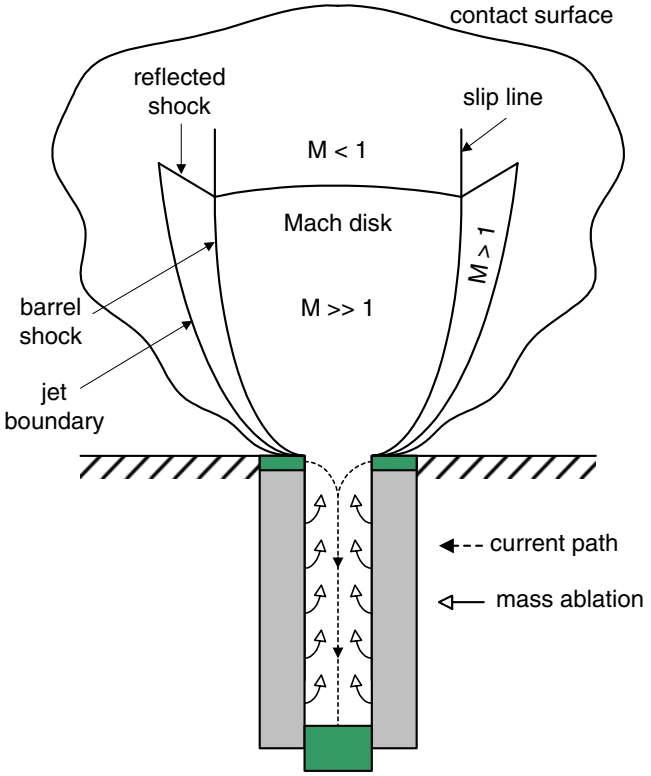

Fig. 3 Shock structure of the external plasma discharge as a supersonic underexpanded plasma jet

2.2 Numerical Model

The time-dependent differential equations for conservation of mass, momentum (in radial and axial directions), and energy are:

$$\frac{\partial \rho}{\partial t}+\frac{1}{r}\frac{\partial}{\partial r}(r\rho u_r)+\frac{\partial}{\partial z}(\rho u_z)=\dot{\rho}_a \quad \text{(Eq 1)}$$

$$\frac{\partial \rho u_r}{\partial t}+\frac{1}{r}\frac{\partial}{\partial r}(r\rho u_r^2)+\frac{\partial}{\partial z}(\rho u_r u_z)=-\frac{\partial P}{\partial r} \quad \text{(Eq 2)}$$

$$\frac{\partial \rho u_z}{\partial t}+\frac{1}{r}\frac{\partial}{\partial r}(r\rho u_z u_r)+\frac{\partial}{\partial z}(\rho u_z^2)=-\frac{\partial P}{\partial z} \quad \text{(Eq 3)}$$

$$\frac{\partial \rho \varepsilon}{\partial t}+\frac{1}{r}\frac{\partial}{\partial r}\left(r\rho u_r\left(\varepsilon+\frac{P}{\rho}\right)\right)+\frac{\partial}{\partial z}\left(\rho u_z\left(\varepsilon+\frac{P}{\rho}\right)\right)=\frac{J^2}{\sigma} \quad \text{(Eq 4)}$$

$$\varepsilon=e+\frac{1}{2}(u_r^2+u_z^2) \quad \text{(Eq 5)}$$

where ρ, P, u_r, u_z, and e are the mass density, pressure, radial velocity, axial velocity, and the specific internal energy, respectively. These equations represent the inviscid compressible gas dynamics. In the energy equation, the term J^2/σ presents the Joule heating inside the capillary bore, where J is the current density ($= I/\pi r_b^2$) and σ is the plasma electrical conductivity. In addition to above equations of four conserved quantities, the distribution of polycarbonate plasma density (ρ_p) is solved simultaneously to determine the mass fraction of air and polycarbonate components.

$$\frac{\partial \rho_p}{\partial t}+\frac{1}{r}\frac{\partial}{\partial r}(r\rho_p u_r)+\frac{\partial}{\partial z}(\rho_p u_z)=\dot{\rho}_a \quad \text{(Eq 6)}$$

The plasma specific internal energy consists of thermal energy, electronic energy, and chemical energy components such as

$$e=\frac{3}{2}(1+\alpha)\frac{kT}{\bar{m}}+e_{el}+e_{chem} \quad \text{(Eq 7)}$$

where α, k, and $\bar{m}$ are the degree of ionization, Boltzmann constant, and average particle mass of the heavy species, respectively. For the equation of state, the following ideal gas approximation is considered:

$$P=(1+\alpha)\rho\frac{kT}{\bar{m}} \quad \text{(Eq 8)}$$

Due to high pressure and high temperature, plasmas are fully dissociated into their elemental constituents and are partially or fully ionized. Also, at such extreme conditions, plasmas are expected to be in local thermodynamic equilibrium. Therefore, the equilibrium compositions of the plasma are determined by considering the following form of the Saha equation:

$$\frac{n_{i+1}n_e}{n_i}=2\frac{Q_{i+1}}{Q_i}\left(\frac{2\pi m_e kT}{h^2}\right)^{3/2}\exp\left(-\frac{I_i-\Delta I_i}{kT}\right) \quad \text{(Eq 9)}$$

where the subscripts i and $i+1$ represent a heavy species and its next ionization level and n_e is the electron number density. The partition functions Q_i can be determined by considering the degeneracy and the energy of electronic excitation level. The term ΔI_i is the correction to the ionization energy of heavy species, I_i for the nonideal plasma behavior (Ref 9). In this study, up to two ionization levels of the monoatomic heavy species are considered. For a partially ionized plasma, the electrical conductivity is determined based on the electron collisions with both neutral atoms and ions and can be expressed as

$$\sigma=\frac{n_e e_c^2}{m_e(\bar{\nu}_{en}+\bar{\nu}_{ei})} \quad \text{(Eq 10)}$$

where $\bar{\nu}_{en}$ is the electron-neutral collision frequency and $\bar{\nu}_{ei}$ is the electron-ion collision frequency. In evaluating $\bar{\nu}_{ei}$, Zollweg and Liebermann model (Ref 12) is implemented for a correction to the traditional Spitzer model to account for nonideal effects in a dense plasma. Electrical conductivity of polycarbonate plasma is shown in Fig. 4 as a function of temperature and pressure. More details in the calculation of thermodynamic and transport properties of plasma vapor can be found in the work of Batteh et al. (Ref 13).

To model the mass ablation from the bore wall due to radiative heating from plasma column, the mass ablation density rate $\dot{\rho}_a$ is introduced in the mass equation as a source term, rather than the mass ablation is treated as the

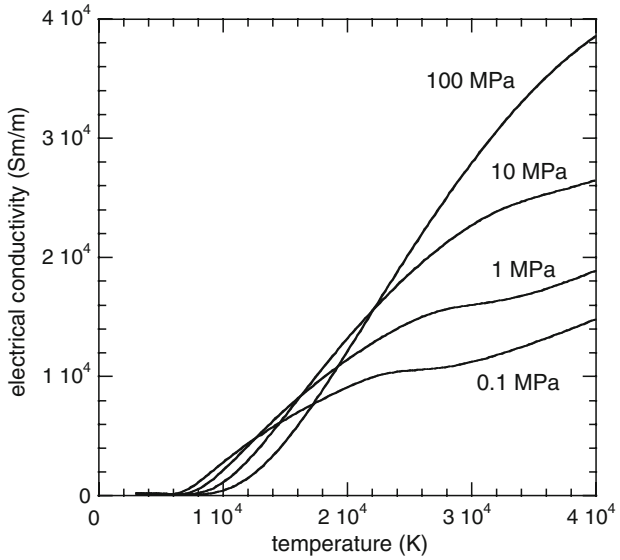

Fig. 4 Electrical conductivity of polycarbonate plasma as a function of temperature and pressure

boundary condition at the bore wall. From the approach using a one-dimensional modeling by Powell and Zielinski (Ref 5, 6), the mass ablation can be approximated by equating the radiative flux from the plasma to the interior wall of the capillary bore and the energy of the ablated material inside the bore. Therefore, $\dot{\rho}_a$ is given by

$$\dot{\rho}_a = \frac{2f\sigma_{sb}T^4/r_b}{\varepsilon + (P/\rho)} \quad \text{(Eq 11)}$$

where σ_{sb} is the Stefan-Boltzmann constant and T is the temperature. In the above equation, the factor f represents the deviation of radiative flux from the blackbody behavior. It might be questionable to use the above expression that was derived from the one-dimensional model in the multidimensional computation such as the present case, but it would be reasonable approximation if the bore length is substantially greater than the bore diameter and subsequently the radial variation of flow properties is negligible compared to the axial variation. It should be pointed out that the two source terms in mass and energy equations are applied only inside the capillary bore. Note that present study neglected the mass ablation from the electrodes and the explosion of the fuse wire. Measurements (Ref 4) show that the fuse wire breaks down within 10 μs from initial current discharge.

2.3 Numerical Solution Procedure

The numerical scheme employed in this article is based on LCPFCT (Ref 14) which uses the one-dimensional FCT (flux-corrected transport) algorithm with fourth-order phase accuracy. This scheme is originally developed by Boris (Ref 15) and basically solves the generalized one-dimensional continuity equation in the form of

$$\frac{\partial\phi}{\partial t} + \frac{1}{r^{n-1}}\frac{\partial}{\partial r}(r^{n-1}\phi u) = \frac{1}{r^{n-1}}\frac{\partial}{\partial r}(r^{n-1}D_1) + C_2\frac{\partial D_2}{\partial r} + D_3 \quad \text{(Eq 12)}$$

where ϕ is the generalized conserved quantity (ρ, ρ_p, ρu_r, ρu_z, $\rho\varepsilon$) and the terms C_2, D_1, D_2, and D_3 accommodate the source terms. The integer n is 1 in axial direction and 2 in radial direction. This scheme has been proven to be highly accurate and efficient, especially in resolving steep gradients and it can be easily extended to the two-dimensional cases by time-step splitting in each coordinate direction. A set of the governing equations in the previous section is separated into two sets for radial and axial coordinates and those two sets are subjected to successive integration along the corresponding directions at each time step.

Axisymmetric computational domain includes the interior region of the capillary bore and the open-air region outside the capillary. Inside the capillary bore, 20 × 100 cells are placed, while the open-air region contains 300 × 500 cells. The size of the open-air computational domain is approximately 40 bore diameters in axial direction and 20 bore diameters in radial direction. Note that the grids are clustered around the bore exit to resolve the steep gradients. The initial condition of the computation is set to be the quiescent air at the standard atmospheric conditions, and the integrating time step is determined by the CFL condition.

3. Results and Discussion

3.1 Plasma Flow in the Capillary Bore of Electrothermal Gun

By numerically integrating the mass ablation density rate, cumulative mass of the bore ablation can be estimated for the entire duration of the plasma firing. In the experiments, capillary bore mass was measured through a series of 32 consecutive firings, and the averaged mass ablation per firing was found to be approximately 7.6 mg (Ref 4). The calculation yields 9.0 mg of mass ablation with the assumption of blackbody radiation ($f = 1$), which is overpredicted but still a reasonable prediction. Deviation factor (f) is found to be 0.85 to match the measured mass ablation and this value is used in the calculations shown here as well as in the previous study.

Figure 5 shows the temporal variation of the calculated plasma conditions at the center of the capillary bore exit plane. At the time of peak current (110 μs), the calculation yields the following peak flow conditions: temperature of 21,800 K, pressure of 26.4 MPa, and mass density of 0.84 kg/m^3. In a previous study (Ref 9), time-dependent one-dimensional modeling with sonic boundary condition at the bore exit was utilized for the inner bore plasma flow. Those results are compared with the present calculations in Fig. 5 and the agreement between two approaches indicates the validity of the sonic condition at the bore exit. To further investigate this matter, plasma velocity and its Mach number at the bore exit are shown in Fig. 6,

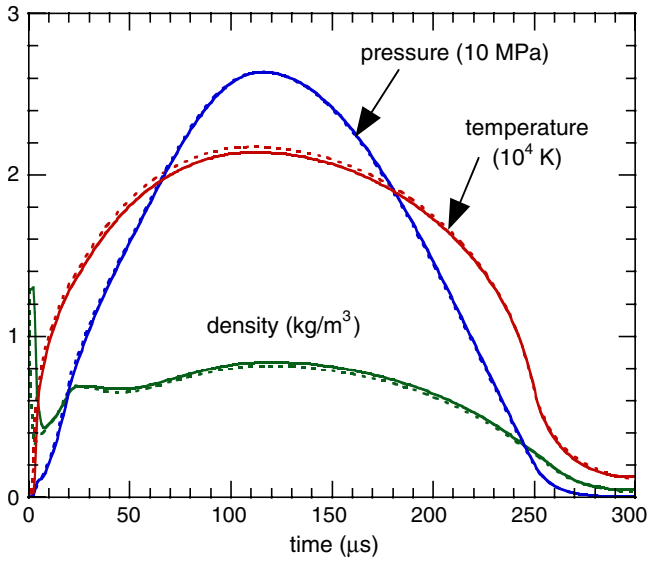

Fig. 5 Calculated plasma conditions at the capillary bore exit. Dotted and solid lines represent the results from one-dimensional plasma bore simulation (Ref 9) and two-dimensional simulation, respectively

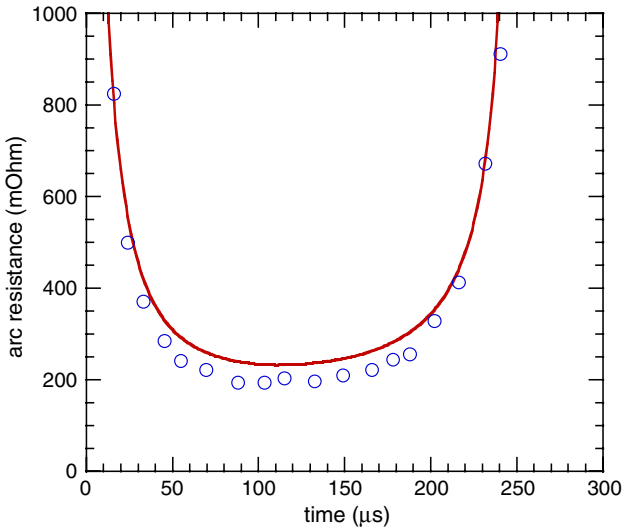

Fig. 7 Transient plasma arc resistance across the capillary bore. Solid line represents the calculation and symbols represent the measurements (Ref 4)

where Mach number is evaluated based on the following speed of sound.

$$c_s = (\gamma_{eff}(1+\alpha)R_h T)^{1/2} \quad \text{(Eq 13)}$$

where R_h is the average gas constant of heavy species. In the above equation, using ideal gas approximation, effective specific heat ratio γ_{eff} is evaluated as

$$\gamma_{eff} = 1 + \frac{P}{\rho e} \quad \text{(Eq 14)}$$

From the Mach number time history, it is observed that the flow at the bore exit becomes choked very rapidly within

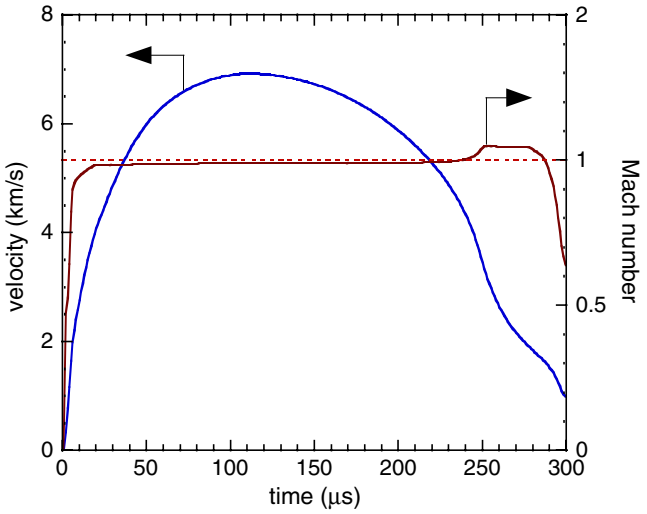

Fig. 6 Calculated flow velocity and Mach number at the center of capillary bore exit plane

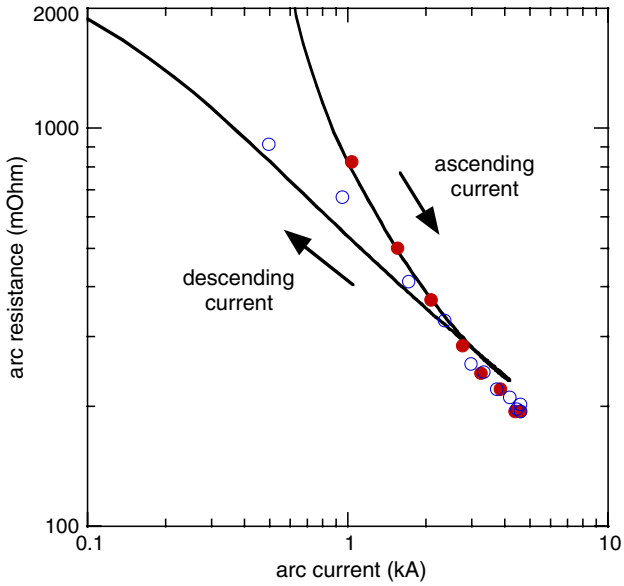

Fig. 8 Plasma arc resistance across the capillary bore with ascending and descending arc current. Solid line represents the calculation and symbols represent the measurements (Ref 4) with ascending (filled) and descending (open) arc current

15 μs. Although the flow is choked, the Mach number at the center of the exit plane is slightly lower than unity, since it is well known that the sonic plane at the exit forms a curvature toward the outer region and does not coincide with the exit plane of choked flow (Ref 16); therefore, the flow remains slightly below sonic at the exit plane. This also explains small discrepancy between two modeling approach, as previously mentioned in the discussion of Fig. 5. Around the end of current discharge from the capacitor at 250 μs, Mach number temporarily exceeds unity and the choked condition loses the identity as the

current discharge fades away. Flow velocity at the bore exit reaches maximum of approximately 6920 m/s at 110 μs.

Plasma arc resistance across the capillary bore is also calculated by averaging the predicted electrical conductivity over the inner volume of the bore and compared quite well with the experimentally determined values in Fig. 7. Additionally, Fig. 8 presents the relationship between arc resistance and arc current showing quasi-steady behavior of arc resistivity at sufficiently high arc current. However, this trend deviates from the quasi-steady behavior at lower current, as illustrated by ascending and descending current in Fig. 8. Arc resistance is considerably higher as the current increases than decreases when the current is not high enough to be in quasi-steady behavior and this is possibly due to the process of establishing the bulk plasma flow in the bore at an early stage of discharge and the incoming energy from the PFN is contributed less into ionizing the plasma flow, resulting in higher arc resistivity. Present prediction is in a favorable agreement with the measurements and simulated this unsteady effect very well.

3.2 Flowfield and Shock Structure of Freely Expanding Pulsed Plasma Jet

Transient evolution of the external plasma discharge is illustrated in Fig. 9 and 10 as Mach number and temperature contours at six different time steps during the discharge duration time. Mach number contours reveal the typical flow pattern of supersonic underexpanded jets featuring strong Mach disk and the barrel shock as well as the propagation of the hemispherical blast wave. Figure 10 includes two flow visualization photos of the experimentally captured visible emission images (Ref 3) for the comparison with the computational results. Although the luminosity of visible emission does not directly represent the temperature field, the comparison shows that the calculated flow pattern and shock structure of the plasma jet is in excellent agreement with the experimental flow visualization. Those visible emission images show the contact surface between the plasma and the background gas in addition to the inner shock structure, and the shape of the contact surface from the flow visualization is very

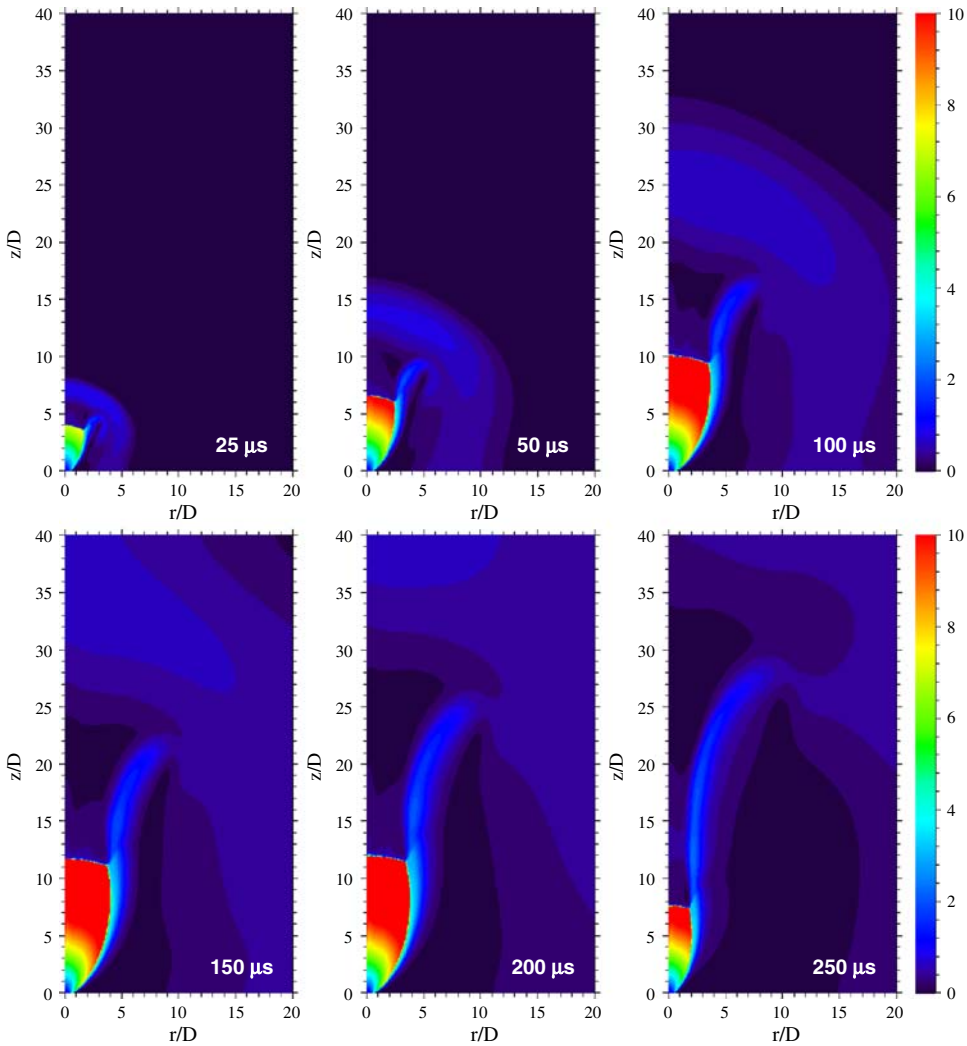

Fig. 9 Mach number contours of the plasma discharge into the open air

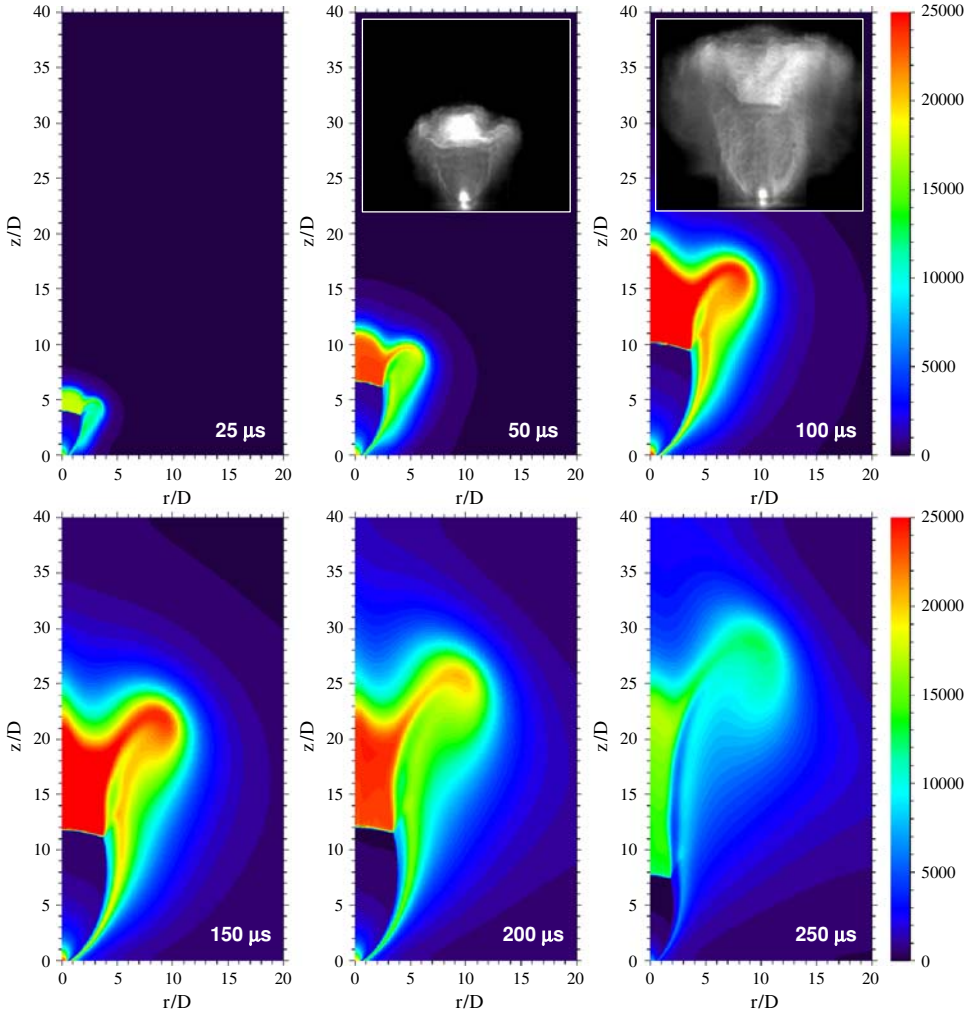

Fig. 10 Temperature contours (in Kelvin) of the plasma discharge into the open air. Two photos of the experimental flow visualization represent the visible emission from the plasma jet (Ref 3). Courtesy of N. T. Clemens and P. L. Varghese

similar to those from the computation including the vortex flow motion around the upper left and right tip of the jet.

Temporal trajectories of the shock structure such as Mach disk and contact surface are determined from those experimental visible emission images (Ref 3) and presented along with the time-space contours of calculated temperature along the axial line in Fig. 11. Note that negative axial coordinate z/D from −10 to 0 represents the axial line in the inner bore. Forwarding and retreating Mach disk location is well simulated and maximum distance of the Mach disk is approximately 11 bore diameters from the bore exit both in the measurements and present calculations. For the contact surface, relatively gradual variation of flow properties across the contact surface makes the comparison difficult in experimental and computational flow visualization; nevertheless, the computation seems to predict the expansion of the contact surface reasonably, judging from the fact that contact surface

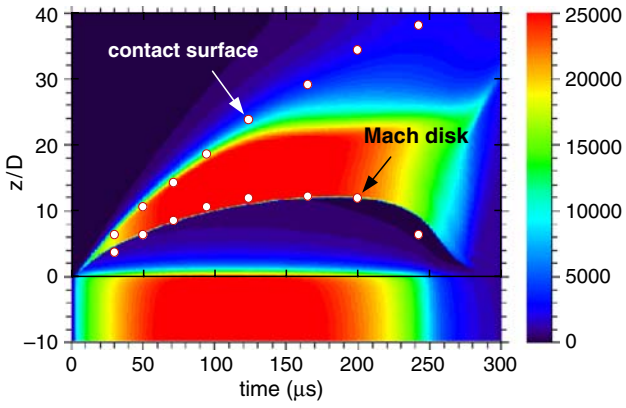

Fig. 11 Time-space contours of temperature along the axial line. Open symbols represent the trajectories of Mach disk and contact surface during the plasma discharge from the measurements (Ref 3)

determined from the experiments agrees well with the contour lines of plasma temperature.

4. Conclusions

The pulsed plasma discharge from the electrothermal gun into the open air has been numerically simulated by solving the time-dependent inviscid gas dynamics equations for the two-dimensional computational domain including capillary bore and the open-air space. The numerical scheme employed the FCT gas dynamics scheme which is based on the FCT algorithm in solving generalized continuity equations. Inside the capillary bore, Joule heating and the mass ablation from the bore wall are modeled. At the bore exit, the computational results verified the choked flow condition as expected. Computed mass ablation from the bore agrees quite well with the experimentally determined mass loss. The flow structure of freely expanding plasma discharge in the open air is essentially the highly underexpanded supersonic jet and many important features such as Mach disk, barrel shock, contact surface, and spherical blast wave are well predicted and compare favorably with the experimental flow visualization.

Acknowledgments

The author greatly acknowledges Professors N. T. Clemens and P. L. Varghese of The University of Texas at Austin for providing their experimental data and valuable suggestions.

References

1. K.J. White, G.L. Katulka, T. Khong, and K. Nekula, ''Plasma Characterization for Electrothermal-Chemical (ETC) Gun Applications,'' ARL-TR-1491, U. S. Army Research Laboratory, Aberdeen Proving Ground, 1997
2. M.J. Nusca, K.J. White, A.W. Williams, A.M. Landsberg, T.R. Young, and C.A. Lind, ''Computational and Experimental Investigations of Open-Air Plasma Discharges,'' AIAA Paper 99-0865, 1999
3. J.M. Kohel, L.K. Su, N.T. Clemens, and P.L. Varghese, Emission Spectroscopic Measurements and Analysis of a Pulsed Plasma Jet, *IEEE Trans. Magn.*, 1997, **35**(1), p 201-206
4. J.U. Kim, N.T. Clemens, and P. L. Varghese, ''Experimental Study of an Underexpanded Pulsed Plasma Jet,'' AIAA Paper 99-0452, 1999
5. J.D. Powell and A.E. Zielinski, ''Theory and Experiment for an Ablating-Capillary Discharge and Applications to Electrothermal-Chemical Guns,'' BRL-TR-3355, U.S. Army Ballistic Research Laboratory, Aberdeen Proving Ground, 1992
6. J.D. Powell and A.E. Zielinski, Capillary Discharge in the Electrothermal Gun, *IEEE Trans. Magn.*, 1993, **29**(1), p 591-596
7. L.L. Raja, P.L. Varghese, and D.E. Wilson, Modeling of the Electrogun Metal Vapor Plasma Discharge, *J. Thermophys. Heat Transfer*, 1997, **11**(3), p 353-360
8. M.F. Zaghloul, M.A. Bourham, and J.M. Doster, Semi-Analytical Modelling and Simulation of the Evolution and Flow of Ohmically-Heated Non-Ideal Plasmas in Electrothermal Guns, *J. Phys. D: Appl. Phys.*, 2001, **34**, p 772-786
9. K. Kim, Time-Dependent One-Dimensional Modeling of Pulsed Plasma Discharge in a Capillary Plasma Device, *IEEE Trans. Plasma Sci.*, 2003, **31**(4), p 729-735
10. E.M. Schmidt and D.D. Shear, Optical Measurements of Muzzle Blast, *AIAA J.*, 1975, **13**(8), p 1086-1091
11. B.E. Djakov and V. Hermoch, Plasma Formation at the Electrodes of Pulsed Arcs, *Vacuum*, 2003, **69**, p 129-132
12. R.W. Liebermann and R.J. Zollweg, Electrical Conductivity of Nonideal Plasmas, *J. Appl. Phys.*, 1987, **62**(9), p 3621-3627
13. J. Batteh, J. Powell, D. Sink, and L. Thornhill, A Methodology for Computing Thermodynamic and Transport Properties of Plasma Mixtures in ETC Injectors, *IEEE Trans. Magn.*, 1995, **31**(1), p 388-393
14. J.P. Boris, A.M. Landsberg, E.S. Oran, and J.H. Gardner, ''LCPFCT—Flux-Corrected Transport Algorithm for Solving Generalized Continuity Equations,'' Naval Research Laboratory Report No. 6410-93-7192, 1993
15. J.P. Boris, ''Flux-Corrected Transport Modules for Generalized Continuity Equations,'' NRL Memorandum Report 3237, Naval Research Laboratory, Washington, D.C., 1976
16. J. Iwamoto, Impingement of Under-Expanded Jets on a Flat Plate, *J. Fluid Eng. Trans. ASME*, 1990, **112**, p 179-184